




Article

Reactive Spark Plasma Sintering and Thermoelectric Properties of Zintl Semiconducting $\text{Ca}_{14}\text{Si}_{19}$ Compound

Doaa Omar A. Ali ^{1,2}, Marco Fabbiani ² , Loïc Coulomb ² , Simon Bosc ², Benjamin Villeroy ³,
Camille Estournès ⁴, Claude Estournès ⁴ , Michael Marek Koza ¹ , Mickaël Beaudhuin ^{2,*} 
and Romain Viennois ^{2,*} 

¹ Institut Laue-Langevin (ILL), 38042 Grenoble, France

² ICGM, Univ. Montpellier, CNRS, ENSCM, Montpellier, France

³ ICMPE-CNRS, Univ. Paris-Est Creteil, 94320 Thiais, France

⁴ CIRIMAT, Université de Toulouse, CNRS, Université Paul-Sabatier, 118 Route de Narbonne, CEDEX 9, 31062 Toulouse, France

* Correspondence: mickael.beaudhuin@umontpellier.fr (M.B.); romain.viennois@umontpellier.fr (R.V.)

Abstract: We present a new reactive spark plasma sintering (RSPS) technique for synthesizing the rhombohedral $\text{Ca}_{14}\text{Si}_{19}$ phase. The RSPS approach reduces the synthesis time from several weeks to a few minutes. The RSPS was found to be sufficient for obtaining a high level of purity of the $\text{Ca}_{14}\text{Si}_{19}$ under a pressure of 100 MPa for a dwell period of 5 min at a temperature of 900 °C. From electrical resistivity measurements, we were able to determine the energy band gap of $\text{Ca}_{14}\text{Si}_{19}$ to $E_g = 0.145(15)$ eV. The Seebeck coefficient shows $\text{Ca}_{14}\text{Si}_{19}$ as a p-type semiconductor at room temperature. It becomes n-type with increasing temperature pointing to significant bipolar and conduction band contributions due to the narrow bandgap of the compound.

Keywords: reactive SPS; thermoelectricity; silicides



Citation: Ali, D.O.A.; Fabbiani, M.; Coulomb, L.; Bosc, S.; Villeroy, B.; Estournès, C.; Estournès, C.; Koza, M.M.; Beaudhuin, M.; Viennois, R. Reactive Spark Plasma Sintering and Thermoelectric Properties of Zintl Semiconducting $\text{Ca}_{14}\text{Si}_{19}$ Compound. *Crystals* **2023**, *13*, 262. <https://doi.org/10.3390/cryst13020262>

Academic Editors: Oliver Oeckler and Andrey Prokofiev

Received: 2 December 2022

Revised: 6 January 2023

Accepted: 25 January 2023

Published: 2 February 2023



Copyright: © 2023 by the authors. Licensee MDPI, Basel, Switzerland. This article is an open access article distributed under the terms and conditions of the Creative Commons Attribution (CC BY) license (<https://creativecommons.org/licenses/by/4.0/>).

1. Introduction

The development of all modern societies significantly relies on energy sources. Consequently, global energy demand is one of the most significant challenges in the 21st century. It contributes significantly to economic, social, and geopolitical instabilities. Furthermore, the use of limited energy sources, such as fissile or fossil fuels (oil, gas, coal, etc.), are associated, respectively, with long-term radioactive contamination or environmental crises such as global climate change and global warming induced by CO_2 emissions. However, these limited energy sources currently provide around 85% of energy supply [1,2]. Therefore, providing a reliable supply of clean, affordable energy is always in high demand. Numerous alternative energy sources, including photovoltaic, wind, geothermal, and thermoelectrics have received particular attention in the last decade. It is known since the nineteenth century that thermoelectric materials (TEMs) are able to convert thermal heat into electricity via Seebeck's effect [3] and vice versa via Peltier's effect [4]. Seebeck's effect attracts high interest for its potential to generate electrical power from waste heat. Therefore, it is expected to significantly contribute to the world's future electrical power management and economy by harvesting waste heat released in industry, transport, and household applications [5,6]. Moreover, thermoelectric modules have many advantages such as the absence of movable elements or cryogenic fluids, compactness, higher reliability, and overall life expectancy. However, the efficiency of thermoelectric modules is much lower than those of conventional electrical power generators with mechanical parts [7]. Indeed, the efficiency of thermoelectric devices is limited to about 10% compared to 30% of modern steam turbines [7]. Thus, the performance of TEMs still requires a significant boost.

Thermoelectric modules are made of two legs made of p-type and n-type materials connected electrically in serial and thermally in parallel. Therefore, both p-type and n-type

TEMs must be optimized. Their efficiency is related to the thermoelectric dimensionless figure of merit (ZT) defined in Equation (1) as

$$ZT = \frac{S^2}{\rho(k_e + k_l)} T \quad (1)$$

with the Seebeck coefficient S , electrical resistivity ρ , absolute temperature T , and the electronic and lattice thermal conductivities k_e and k_l , respectively [8]. Equation (1) clearly underlines that a high power factor S^2/ρ and low thermal conductivities k_e and k_l are the key features for high ZT numbers. Thereby the parameters k_e and S^2/ρ are bound by electronic conditions placing TEMs into the regime of semiconductors and semi-metals.

Most of the best TEMs and notably Bi_2Te_3 and PbTe are semiconducting materials with narrow energy bandgaps smaller than 0.5 eV, allowing for a ZT higher than 1 [6]. The optimal charge carrier concentration for optimizing these types of materials is in the 10^{19} – 10^{20} cm^{-3} range [9], although some poor metals with both a highly dispersive band and a flat band, such as filled skutterudites, can also have large power factors [10]. Another way of improving the power factor is to lower the dimensionality of the TEMs. Lattice thermal conductivity can be reduced in different ways. Following Glenn Slack, excellent thermoelectric performance can be achieved in materials by respecting the electron crystal and phonon glass concept [11]. Semiconducting compounds with complex crystal structures made of a high number (N) of atoms per primitive unit cell meet this concept closely. Since the main carriers of the heat are acoustic phonons, however, they represent, only $1/N$ of the total vibrational spectrum in such complex compounds. Moreover, high structural complexity often leads to reduced phonon velocities as well as to high phonon-phonon scattering due to strong interactions of acoustic with low-energy optical modes [11–14]. This effect can be particularly well triggered by alloying TEMs with heavy elements. Other sources of enhanced phonon scattering can be static in nature such as defects, dopants, or interfaces in nanostructured materials.

The majority of today's best-performing and purchasable TEMs are made from rare [15], hence expensive, and often toxic chemical elements [9,16–19]. Alkaline-earth silicide compounds offer a unique opportunity to overcome these cost and hazard issues. As an example, calcium silicides are made up of the fifth (Ca) and second (Si) most abundant elements in the earth's crust [15,20]. Hence, they are cheap, and additionally, they are non-toxic. As many of the calcium silicide compounds are equally semiconducting and have a complex crystal structure, they fulfill all necessary requirements to become the next generation of environment-friendly TEMs.

Only a few alkaline-earth silicides have been investigated for their TEM capability. As far as we know, the calcium–silicide family consists of six members in the equilibrium phase diagram: orthorhombic CaSi [Cmcm, No 63], rhombohedral CaSi_2 [R-3m, No 166], tetragonal Ca_5Si_3 [I4/mcm, No 140], orthorhombic Ca_2Si [Pnma, No 62], hexagonal Ca_3Si_4 [P6₃/m, No 176], and rhombohedral $\text{Ca}_{14}\text{Si}_{19}$ [R-3c, No 167] [21–30]. In addition to the stable R6 rhombohedral CaSi_2 phase with 6 layers stacking, there is a metastable R3 rhombohedral CaSi_2 phase [R-3m, No 166] with 3 layers stacking that can be obtained from the sintering of R6 CaSi_2 under H_2 atmosphere or from thin film epitaxial growth [31,32]. The R6 rhombohedral CaSi_2 phase undergoes two structural phase transitions under high pressure and below 700 K, to a trigonal [P-3m1, No 164] phase between 8 and 16 GPa and to a hexagonal phase [P6/mmm, No 191] above 16 GPa [33,34]. Under high-pressure and high-temperature conditions, a tetragonal CaSi_2 phase [I4₁/amd, No 141] was obtained above 4 GPa [33–35]. All the CaSi_2 polymorphs are metallic [31,33,36] and the different high-pressure phases are superconducting at low temperatures [33]. Other Si-rich calcium silicide phases were obtained under high-pressure and high-temperature conditions such as tetragonal CaSi_3 [I4/mmm, No 139] [37] from 12 GPa and orthorhombic CaSi_6 [Cmcm, No 63] [38] at 10 GPa. Both compounds are metallic, the first one being superconducting below 4.5 K [37] whereas the last one is formed of channels where Ca atoms are intercalated [38]. Among all the other calcium silicide compounds, density functional theory (DFT) calculations show that

only Ca_2Si , Ca_3Si_4 , and $\text{Ca}_{14}\text{Si}_{19}$ are semiconducting compounds [28,39–42]. Orthorhombic Ca_2Si is semiconductive with a direct energy bandgap of about 0.88 eV, recently reported from optical spectra of a Ca_2Si thin film on sapphire substrate [32], which is slightly lower than the value of 1.02 eV found with GW calculations, a post-DFT method that corrects the energy bandgap obtained from the DFT method [40]. Growth of thin films has been performed for applications such as light-emitting diodes in the near-infrared range [32]. Thermoelectric and electrical transport experiments on orthorhombic Ca_2Si [43,44] showed that it is p-type and that the electrical conductivity (σ) is too weak, even after doping with Na, and that the energy activation found is much smaller than the energy bandgap found from the optical experiments [32]. Concerning Ca_5Si_3 , there are several contradicting results. Jun et al. [45] reported an energy bandgap of 0.65 eV from infrared absorption on a badly crystallized thin film of Ca_5Si_3 , but there was still a strong absorption signal below this energy in their data, which cast doubts about their conclusions. Inaba et al. [46] and Wen et al. [43] both reported an increase in electrical conductivity (σ) with temperature, whereas Uhera et al. [47] found an almost independent behavior and Imamura et al. [48] found a decrease of the electrical conductivity (σ) at higher temperatures characteristic of metals that is in agreement with DFT calculations [41]. Ca_5Si_3 is of p-type and its Seebeck coefficient varies from 30 $\mu\text{V/K}$ to 90 $\mu\text{V/K}$, depending on the different works [46–48]. Imamura et al. [48] reported a rather large power factor of about $0.6 \text{ mWm}^{-1}\text{K}^{-2}$ and a moderate ZT of 0.11 at 950 K for Ca_5Si_3 . CaSi and R6 rhombohedral CaSi_2 have Seebeck coefficients of few $\mu\text{V/K}$, typical of metals, with a negative sign for CaSi [47,48].

Ca_3Si_4 and $\text{Ca}_{14}\text{Si}_{19}$ are of particular interest as they are semi-conducting valence-charge-balanced Zintl phases with complex crystal structures [39,49]. Ca_3Si_4 is a low-temperature phase whereas $\text{Ca}_{14}\text{Si}_{19}$ is a high-temperature phase, and both phases coexist between 900 °C and 930 °C [39]. The electronic energy bandgaps were approximated for Ca_3Si_4 and $\text{Ca}_{14}\text{Si}_{19}$ from DFT calculations. Different DFT studies concluded that Ca_3Si_4 has indirect bandgaps of 0.35 eV [42] and 0.56 eV [39]. The bandgap for $\text{Ca}_{14}\text{Si}_{19}$ was found from DFT to be 0.02 eV [39] and experimentally to be 0.12 eV [21]. The Seebeck coefficients of Ca_3Si_4 and $\text{Ca}_{14}\text{Si}_{19}$ at room temperature are 42 $\mu\text{V/K}$ and -183 V/K , respectively, but the electrical conductivity (σ) at room temperature of Ca_3Si_4 is low [39]. Their thermoelectric properties must be studied in order to conclude their TEM potential. According to the phonon glass electron crystal concept [11–14], their structural complexity should facilitate low k_1 values and enhance ZT appreciably. The drawback of the structural complexity is, however, a difficult synthesis process that comprises long-time annealing for several weeks for bulk materials [39], and only very recently thin films containing significant amounts of $\text{Ca}_{14}\text{Si}_{19}$ in addition to CaSi_2 have been obtained [32]. As a consequence, while the elements Ca and Si are abundant and cheap, their casting into semiconducting thermoelectric compounds has been tedious, long-lasting, and expensive.

This work aims to pave a new way of synthesizing calcium–silicide compounds. We show a new approach to reduce the time, energy, and thus costs needed to synthesize the rhombohedral $\text{Ca}_{14}\text{Si}_{19}$. This is accomplished by the application of the reactive spark plasma sintering (RSPS) technique [50,51].

Spark plasma sintering (SPS) is an advanced powder metallurgy technique belonging to the family of electrical current-assisted sintering technologies, is a more than 30-year-old advanced sintering process for generating quick powder consolidation–densification, employing a high-intensity pulsed direct current under high uniaxial pressure [50,52]. It became more widespread for the rapid elaboration–densification of all classes of materials (metals, ceramics, and polymers) and their composites because of several advantages over more conventional techniques such as pressureless sintering and hot-pressing, including lower sintering temperatures, higher heating rates, and shorter holding times. This may somehow influence/change the mechanisms involved in the sintering (in densification and/or grain growth stages) of the materials. The development of SPS is still in progress. High-pressure SPS, SP-texturing, and -extrusion have recently been proposed, but the most important progress of the process was achieved with the lifting of one of the techno-

logical locks with the development of strategies to develop 3D near-net-shape materials by SPS [53,54]. Sintering involves kinetics and thermodynamics effects; more recently, flash-SPS (with heating rate up to several thousand of °C/min) and cold-SPS (densification at a temperature lower than 400 °C) have been developed to control the microstructures (grain size, porosity rate, and size, as well as the nature and size of the grain boundaries) of the densified materials [55,56]. Even though specific SPS mechanisms have not been clearly evidenced and generalized, studies have shown that the combination of thermal, electrical, and pressure effects have huge impacts on the structure, the microstructures, and, as a consequence, on the properties of the materials thus obtained. Depending on the nature of the starting material and the technique used, up to three driving forces may be involved to reduce the free energy of the system when conventional sintering occurs: the curvature of the particulate surfaces, externally applied pressure, and chemical reaction [57]. The chemical reaction can be of a different nature (dehydration or decomposition of precursors, reaction of a mixture of elemental or binary compounds, etc.) and may occur during the SPS process which is then RSPS [50,51,58]. This strategy has been applied in particular to sinter refractory materials like borides, carbides, and their composites, or materials of complex compositions such as MAX phases [59] and high-entropy materials [60]. In the case of an exothermic reaction, self-sustained RSPS can achieve an even quicker synthesis, but it is more difficult to manage than conventional RSPS [51]. The utilization of small-sized grains, such as those obtained through ball milling, can improve the reaction in RSPS [50,51,58].

We report a process to form dense $\text{Ca}_{14}\text{Si}_{19}$ pellets by combining short-time mechanical milling (5 min) with the RSPS approach. The quality of the synthesis products was followed by X-ray diffraction experiments and the final specimens were characterized for their thermoelectric properties and their hardness. Note that the scope of the discussed RSPS approach can be conveniently extended to synthesize other incongruent phases as previously observed on $\beta\text{-FeSi}_2$, while avoiding longtime annealing [58].

2. Material and Methods

2.1. Synthesis of $\text{Ca}_{14}\text{Si}_{19}$

High-purity Ca granules (99.5% Alfa Aesar) and Si lumps (99.9999% Alfa Aesar) were used to prepare 0.4–0.5 g of Ca-Si pre-alloy buttons in an arc melting furnace (Welding Concept, France) under an argon atmosphere. The samples' homogeneity was improved by melting the samples twice. A slight excess of Ca was added to compensate for its evaporation during the melting process. An agate mortar and pestle were used to grind the formed buttons into fine powders. The purest pre-alloy samples obtained from this process were selected by means of X-ray diffraction data. They were sealed under argon in a jar with three 15 mm diameter balls, both made of tungsten carbide. The samples were mechanically milled for 5 min without pauses. We applied a speed of the grinding bowls of ≈ 740 rpm and a speed of the supporting disc of ≈ 370 rpm, corresponding to an acceleration speed of ≈ 5 g in a planetary micro-mill "Pulverisette 7" (Fritsch, Germany).

The reactive spark plasma sintering (RSPS) technique was used to prepare dense pellets using a "Dr Sinter 515S Syntex" machine (Fuji Electronic Industrial Co., Ltd., Japan). Graphite dies (ISO 68 Toyo Tanso) with 8 mm inner diameters were used for these experiments, along with a graphite foil as a protective layer between the sample and the die to increase the lifetime of this latter and for easy removal of the sample. Prior to the experiment, the system was purged with argon gas and the experiment was performed under a primary vacuum (residual cell pressure $P = 10$ Pa). Uniaxial pressure (100 MPa) was applied at room temperature and all along the thermal cycle and DC pulses were delivered by the graphite punches. The temperature was increased to 900 °C at 100 °C/min, this temperature was then maintained for a dwell of 5 min. Cooling was applied down to room temperature (100 °C/min) and the uniaxial load was gradually released during the same time. The temperature was controlled by a K-type thermocouple incorporated in the mold, close to the sample area. The pattern for the applied pulsed direct current delivered

by the SPS machine was a set of 12 consecutive pulses of 3.3 ms each, with a pause of 6.6 ms between pulse sets.

2.2. Sample Characterization

After arc-melting and RSPS treatment, the intermediate and final products were analyzed by X-ray diffraction (X'Pert Pro from Malvern Panalytical in the UK, Cu-K α radiation 1.5406 Å with an accelerated detector PW3050/60 at 45 kV and 30 mA settings). The X-ray data were refined using the Rietveld method with the FullProf software [61]. The chemical homogeneity and composition of the samples were checked using an energy dispersive analyzer of X-ray (EDX) S4800 mounted on an S2600N scanning electron microscope (SEM), both from Hitachi, Japan. Prior to the experiments, the samples were mirror-polished using absolute ethanol as a solvent to avoid surface oxidation. A pellet of diameter 8 mm and thickness 1.456 mm (specimen 1) with a Ca₁₄Si₁₉ content of weight percentage ~89% was selected for measurements of the electrical resistivity ρ [62], and Seebeck coefficient [63] in the temperature range 325 to 650 K. We used homemade equipment, working under vacuum conditions ($\approx 2.10^{-3}$ mbar) for both experiments. The Van der Pauw method was chosen for the ρ measurements [62]. The pellet's macroscopic density was determined with Archimedes' method by measuring both the mass of the pellet in the air and in absolute ethanol. Each sample was measured 10 times for statistics and it was then compared with the microscopic density obtained by the Rietveld refinement. Vickers micro-hardness experiments were performed on a small piece from a pellet (specimen 2) with Ca₁₄Si₁₉ content of weight percentage ~98% (see below for details) by using a micro-hardness testing machine HM-220 (Mitutoyo, Japan) with two different 0.1 and 0.2 kg loads applied during 10 s. In each case and for both faces of the sample, 10 measurements were performed and the average value is reported in GPa.

3. Results and Discussion

3.1. Sintering Process and Phase Stability of Ca₁₄Si₁₉

A large amount of Ca₁₄Si₁₉ was obtained after arc melting; however, significant percentages of secondary phases such as CaSi and CaSi₂ were also detected. Figure 1a shows a typical X-ray pattern on a powdered sample immediately after arc melting. The weight fractions of Ca₁₄Si₁₉, CaSi, and CaSi₂ were 0.630, 0.210, and 0.160, respectively. Figure 1b shows an X-ray pattern on the pellet of specimen 1 immediately after RSPS with no CaSi detected. The weight fraction of CaSi₂ was reduced to 0.046, but a small quantity of CaO phase appeared with a weight fraction of 0.068. Despite our efforts, it was not possible to obtain oxygen-free samples. The sintering displacement curve of specimen 1 is given in Figure 2, with data recorded every second. From Figure 2, we observe a slight shrinkage between 250 °C and 650 °C and a much higher shrinkage between 650 °C and 750 °C. We conjecture that the shrinkage between 250 °C and 650 °C could be due to granular rearrangement and that the sintering occurs mainly in the shrinkage between 650 °C and 750 °C where the shrinkage rate is the largest (0.35 mm/s at 711 °C). Dwelling at a temperature of 900 °C was chosen to complete the reaction. This temperature is far below the peritectic transition at 1085 °C, in which Ca₁₄Si₁₉ decomposes into CaSi and a liquid phase. Note that pellets with high Ca₁₄Si₁₉ content proved to be somewhat brittle. In some RSPS runs we formed pellets with a Ca₁₄Si₁₉ purity higher than weight percentage 98% as shown in the X-ray pattern on the pellet of specimen 2 in Figure 1c. Those pellets broke after extraction from the mold due to residual stresses, which are a consequence of rapidly decreasing temperature, and their brittle nature.

The macroscopic density of the pellets was found to be >99% of the microscopic density. The SEM picture in Figure 3 shows little black regions corresponding to pores in the pellets, confirming their high density. The presence of white spots corresponds to tungsten carbide contamination from the mechanical milling process. Their amount is negligible and does not affect the thermoelectric properties. Larger dark regions are also visible. EDX analysis performed found higher Si content in these regions than expected

for $\text{Ca}_{14}\text{Si}_{19}$, which is in line with the presence of the secondary phase CaSi_2 in addition to $\text{Ca}_{14}\text{Si}_{19}$. Within the region free of secondary phases, we observe good homogeneity of the 14:19 stoichiometry. From the EDX analysis, we determine the stoichiometry to be $\text{Ca}_{14.08}\text{Si}_{19}$ with a standard deviation of less than 0.6%, which is within the accuracy of the experiment.

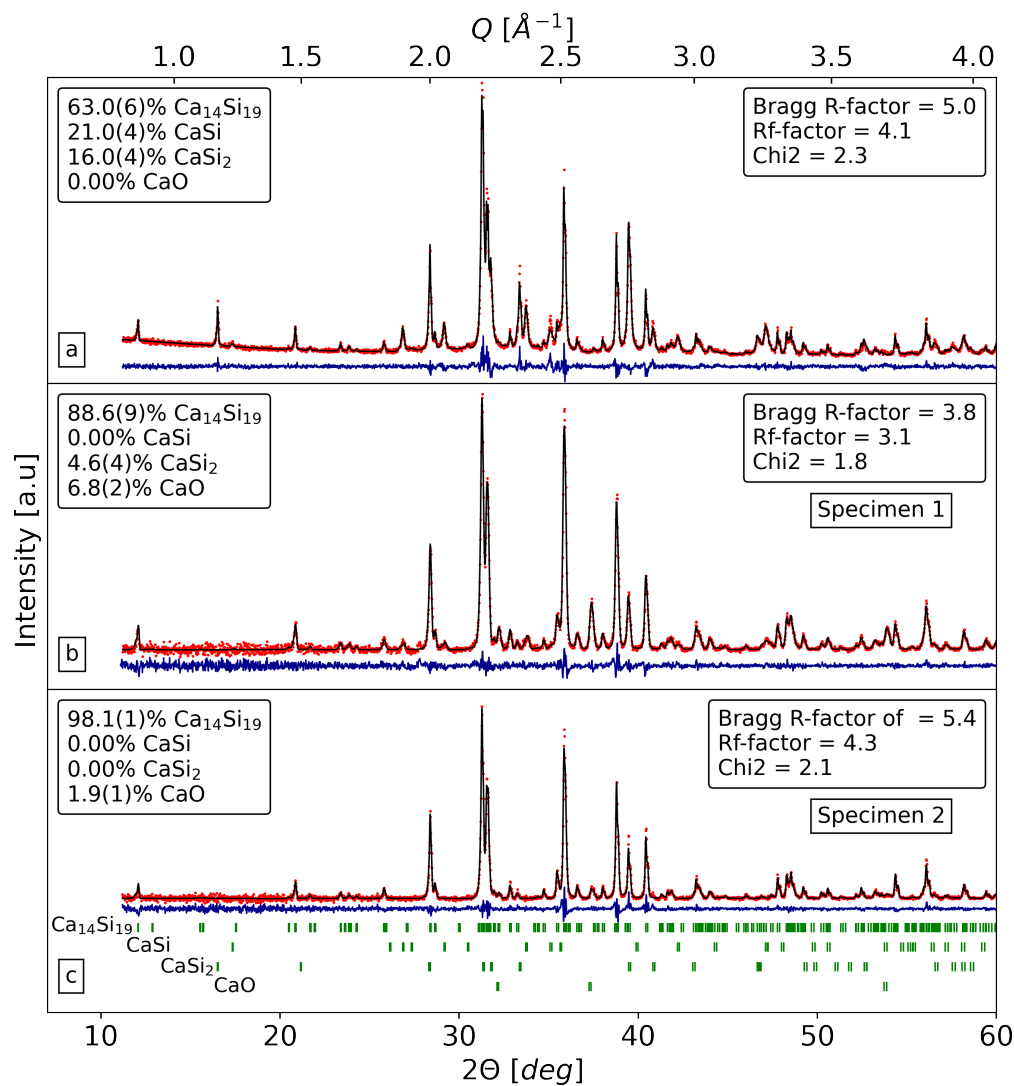


Figure 1. X-ray diffraction and Rietveld refinement results for specimens after arc melting (a), after RSPS for specimen 1 giving a weight percentage of $\sim 89\%$ of $\text{Ca}_{14}\text{Si}_{19}$ (b), and for specimen 2 giving the weight percentage of $\sim 98\%$ of $\text{Ca}_{14}\text{Si}_{19}$ (c). The figure shows the X-ray data (red points), Rietveld profile (black solid lines), the difference between both (dark blue lines), and the Bragg peak positions for the phases identified in the specimens (green tick marks). The relative compositions of the specimens and the fit quality factors (Bragg R-factor and RF-factor are for the $\text{Ca}_{14}\text{Si}_{19}$; Chi2 factor for the entire refinement) are shown to the left and right, respectively.

The Rietveld-fitted lattice parameters of the $\text{Ca}_{14}\text{Si}_{19}$ phase in the different specimens are reported in Table 1 and the corresponding fractional positions of the atoms of specimen 2 after the RSPS process are listed in Table 2. The derived lattice parameters are in good agreement with experimental data recorded at room temperature and published in the literature ($a = b = 8.6707(1) \text{ \AA}$, $c = 68.4864(8) \text{ \AA}$ [39]). We attempted to estimate the occupation numbers of the non-equivalent sites in the $\text{Ca}_{14}\text{Si}_{19}$ phases. No systematic or noteworthy deviations from the nominal site occupancies were identified.

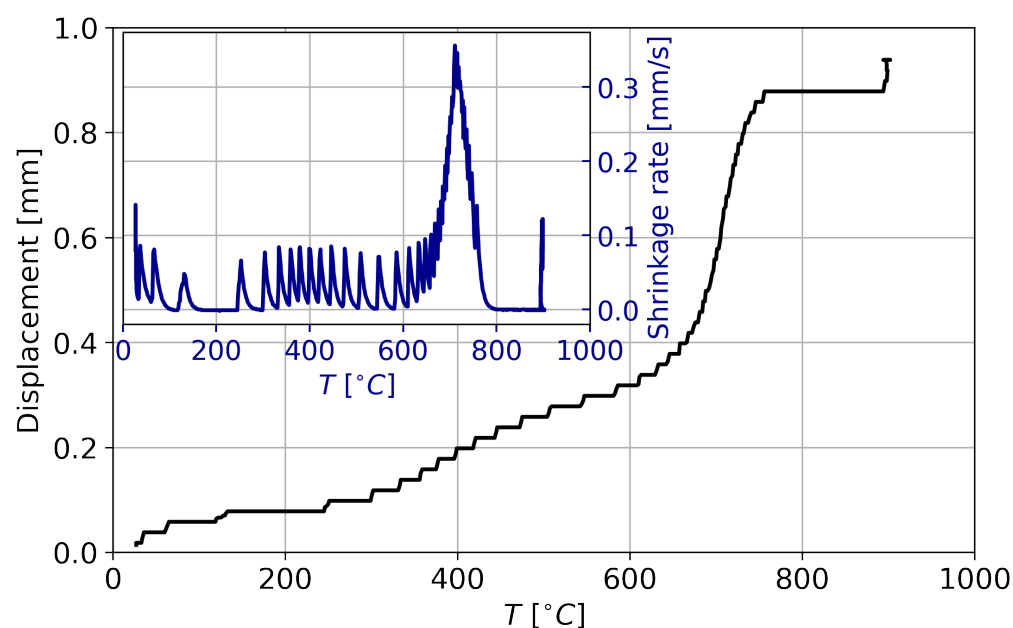


Figure 2. Temperature-dependent displacement curve (black solid line) recorded during the sintering process of specimen 1. Inset highlights the derived corresponding shrinkage rate (blue solid line).

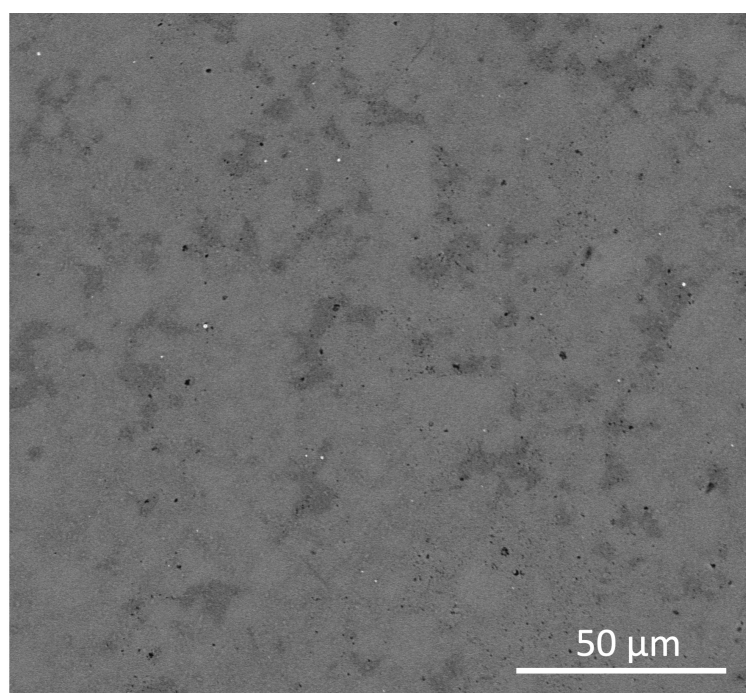


Figure 3. SEM image (backscattered electron detector) of specimen 1 sintered at 900 °C under 100 MPa for 5 min. Few black and white spots as well as dark gray areas correspond to signals from voids, tungsten carbide, and regions with higher Si content, respectively.

Table 1. Lattice parameters of $\text{Ca}_{14}\text{Si}_{19}$ specimens determined from Rietveld fitting analysis of the X-ray diffraction data after the arc melting and the RSPS process.

Specimen	$a = b$ [Å]	c [Å]	V [Å ³]
After Arc Melting	8.6712(3)	68.4789(24)	4458.1(3)
RSPS-Specimen 1	8.6710(4)	68.4761(34)	4459.7(4)
RSPS-Specimen 2	8.6698(2)	68.4707(19)	4456.4(2)

Table 2. Fractional positions of Ca₁₄Si₁₉ specimen 2 after RSPS processing determined from Rietveld fitting analysis of the X-ray diffraction data.

Atoms	x	y	z
Ca(6b)	0	0	0
Ca(12c)	0	0	0.5552(1)
Ca(12c)	0	0	0.6101(1)
Ca(18e)	0.2505(8)	0	0.2500(0)
Ca(36f)	0.0071(6)	0.2488(7)	0.1869(5)
Si(12c)	0	0	0.6527(2)
Si(12c)	0	0	0.7184(2)
Si(18e)	0.5785(12)	0	0.2500(0)
Si(36f)	0.0679(10)	0.3081(8)	0.1426(8)
Si(36f)	0.3846(7)	0.0609(8)	0.0533(9)

3.2. Thermoelectric and Mechanical Properties

We present results from temperature-dependent measurements of electrical resistivity (ρ) and Seebeck coefficient (S) in Figure 4. The electrical resistivity shows a temperature variation characteristic of semiconductors. It decreases from ≈ 4.5 to ≈ 1 m Ω ·cm upon heating from 50 to 400 °C. Assuming a temperature-activated conduction process, we derive from an Arrhenius fit an electronic bandgap of $E_g = 0.145 \pm 0.015$ eV, which is in reasonable agreement with the experimental value of 0.12 eV reported in the literature [21]. In prior calculations, we have found that Ca₁₄Si₁₉ has an indirect bandgap with the valence band maximum along the Γ -L line and the conduction band minimum at the X point [39].

As expected from the narrow bandgap, the Seebeck coefficient is small. Interestingly, it changes its sign at about 100 °C, decreasing from +12 to -16 μ V/K upon heating. We exclude the possibility that the sign change of the Seebeck coefficient is due to a phase transition or oxidization of the specimen since high-temperature X-ray diffraction experiments performed on Ca₁₄Si₁₉, obtained by conventional longtime annealing did not reveal any sign of structural changes up to 873 K [64]. We similarly do not expect any significant contribution of the secondary phases in the electrical transport and thermoelectric properties because CaO is an insulator while CaSi₂ is a metal with a low negative Seebeck coefficient of -7 μ V/K that is independent of temperature [47]. In addition, neither of the two phases is present in sufficient quantity to contribute to the electronic transport.

The sign change of the Seebeck coefficient should be due to a significant contribution arising from an increase in the electronic charge carrier minority concentration. Indeed, as Ca₁₄Si₁₉ is a narrow gap semiconductor, let us consider the case of a two-band model, taking into account both conduction and valence bands [65]. In this case, one can express the total electrical conductivity (σ_{tot}) as $\sigma_{tot} = \sigma_e + \sigma_h$, where σ_e and σ_h are the electrical conductivities from the conduction and valence bands, respectively. Therefore the total Seebeck coefficient (S_{tot}) is defined in Equation (2) as [65]

$$S_{tot} = \frac{\sigma_e S_e + \sigma_h S_h}{\sigma_e + \sigma_h} \quad (2)$$

with the Seebeck contributions S_e and S_h from the conduction and valence bands, respectively. As can be seen from the band structure of Ca₁₄Si₁₉ reported by Moll et al. [39], the conduction band is very flat, whereas the valence band is much more dispersive, although being degenerated several times along different directions. Thus, the effective mass of the electrons m_e^* must be much larger than the effective mass of the holes m_h^* . Since the larger the effective masses of the charge carrier, the larger the Seebeck coefficient, S_e must be much larger than S_h . Therefore, when the minority charge carrier concentration

increases with the temperature, their electrical conductivity follows as well. In $\text{Ca}_{14}\text{Si}_{19}$, the electrons are the minority charge carriers but have larger Seebeck coefficient S_e . Thus, when σ_e increases sufficiently with temperature, the sign change of the Seebeck coefficient happens.

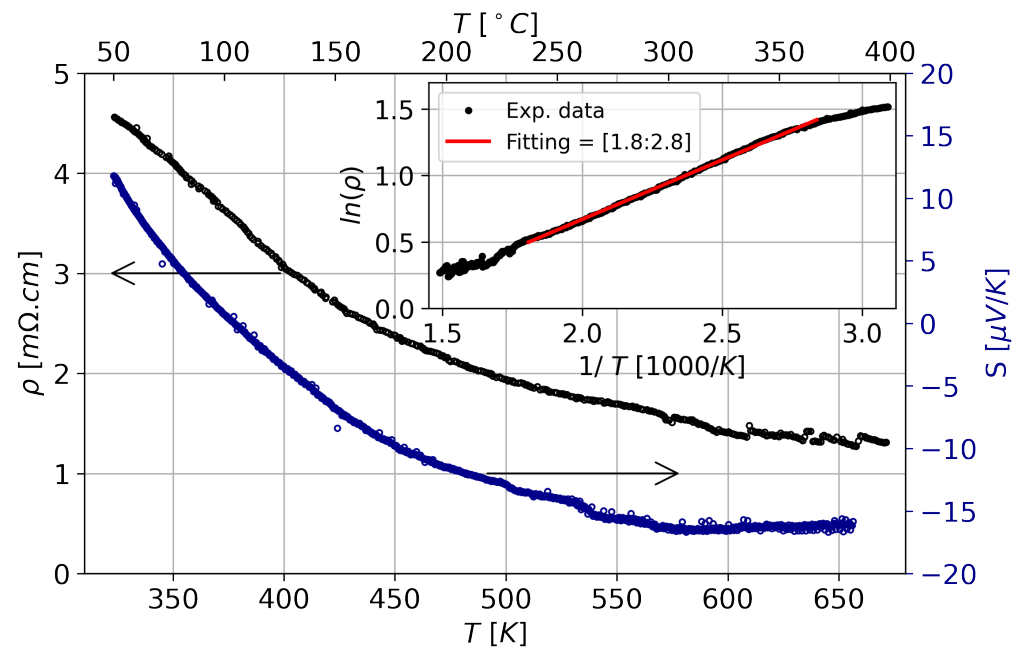


Figure 4. Temperature dependence of electrical resistivity ρ (black open circles, left y-axis indicated by the left arrow) and Seebeck coefficient (S) (dark blue open circles, right y-axis indicated by the right arrow) measured after RSPS. Inset highlights ρ data in an Arrhenius presentation. The red solid line indicates the result of a linear fit to the data representing an activation energy $E_g \approx 0.145 \pm 0.015$ eV.

However, to reduce the electrical resistivity (ρ) and the contribution from minority charge carriers and thus to increase the absolute Seebeck coefficient (S), it will be necessary to dope $\text{Ca}_{14}\text{Si}_{19}$ with appropriate elements. Alkaline metals have a low melting point and high partial pressure and their handling is thus challenging within the arc melting furnace used in this synthesis process. Sealed refractory tubes could be employed, which could avoid problems associated with elements boiling off at high temperatures. Such difficulties would not be observed in synthesizing with aluminum or yttrium for p-type and n-type doping, respectively, as these elements have higher melting points and lower partial pressure.

Until now, only a few alkaline-earth silicides have been investigated for their mechanical properties. Vickers hardness has been reported for the two semiconducting silicides Mg_2Si (4–4.4 GPa) and BaSi_2 (9.11 GPa) [66]. We have determined the Vickers hardness on specimen 2 of $\text{Ca}_{14}\text{Si}_{19}$ to be 6.0 ± 0.5 GPa. It is thus located between the values of Mg_2Si and BaSi_2 [66].

4. Conclusions

Dense $\text{Ca}_{14}\text{Si}_{19}$ pellets can be formed from a Ca-Si pre-alloy formed by arc melting followed by combining mechanical milling with the reactive SPS technique. The sintering conditions for obtaining a high level of purity for the $\text{Ca}_{14}\text{Si}_{19}$ specimens are 100 MPa at 900 °C for a dwell duration of 5 min.

From electrical resistivity (ρ) experiments, we have found an electronic energy bandgap that agrees reasonably well with the values previously reported [21]. The Seebeck coefficient (S) for $\text{Ca}_{14}\text{Si}_{19}$ indicates the large contribution from the minority charge carriers, which should be due to the narrow bandgap and a large Seebeck of the minority charge carriers. Doping will be necessary to reduce the contribution from the minority charge carriers and

to increase both the Seebeck coefficient and the electrical conductivity. Finally, we find that the hardness of $\text{Ca}_{14}\text{Si}_{19}$ is about 6 GPa.

Author Contributions: Conceptualization, D.O.A.A., M.M.K., M.B., and R.V.; methodology, D.O.A.A., M.F., C.E.(Claude Estournès), C.E.(Camille Estournès), M.M.K., M.B., and R.V.; formal analysis, D.O.A.A., M.F., C.E.(Claude Estournès), C.E.(Camille Estournès), M.M.K., M.B., and R.V.; investigation, D.O.A.A., L.C., M.F., C.E.(Claude Estournès), C.E.(Camille Estournès), B.V., S.B., M.M.K., M.B., and R.V.; resources, B.V., C.E.(Claude Estournès), L.C., M.B., and R.V.; writing—original draft preparation, D.O.A.A., M.M.K., M.B., and R.V.; writing—review and editing, D.O.A.A., M.M.K., M.B., and R.V.; visualization, M.M.K., M.B., and R.V.; supervision, M.M.K., M.B., and R.V.; project administration, M.M.K., M.B., and R.V.; funding acquisition, M.M.K., M.B., and R.V. All authors have read and agreed to the published version of the manuscript.

Funding: This work was funded by Institut Laue-Langevin (ILL)—71 avenue des Martyrs CS 20156, 38042 GRENOBLE Cedex 9—France.

Data Availability Statement: Original data are available on reasonable request.

Acknowledgments: The authors would like to thank A. Viera E Silva for his technical support and A. Wildes for proofreading the manuscript. Institut Laue-Langevin (ILL), and Institute Charles Gerhardt Montpellier for supporting this project with the required fund and resources.

Conflicts of Interest: The authors declare that they have no known competing financial interests or personal relationships that could have appeared to influence the work reported in this paper.

References

1. Buchal, C. The challenge of discussing energy facts and climate change. *EPJ Web Conf.* **2020**, *246*, 00003. [\[CrossRef\]](#)
2. Kalghatgi, G. Is it really the end of internal combustion engines and petroleum in transport? *Appl. Energy* **2018**, *225*, 965–974. [\[CrossRef\]](#)
3. Seebeck, T.J. *Magnetische Polarisation der Metalle und Erze durch Temperatur-Differenz*; Abhandlungen Der Deutschen Akademie Der Wissenschaften Zu Berlin, 1822–1823; W. Engelmann: Leipzig, Germany, 1895; pp. 265–373.
4. Peltier, J. Nouvelles expériences sur la calorité des courants électriques. *Annal. Chim. Phys.* **1834**, *56*, 371–386.
5. Ong, K.; Jiang, L.; Lai, K. *Thermoelectric Energy Conversion*; Comprehensive Energy System; Elsevier: Amsterdam, The Netherlands 2018. [\[CrossRef\]](#)
6. Beretta, D.; Neophytou, N.; Hodges, J.; Kanatzidis, M.; Narducci, D.; Martin-Gonzalez, M.; Beekman, M.; Balke, B.; Cerretti, G.; Tremel, W.; et al. Thermoelectrics: From history, a window to the future. *Mater. Sci. Eng. R Rep.* **2019**, *138*, 210–255.
7. Vining, C. An inconvenient truth about thermoelectrics. *Nat. Mater.* **2009**, *8*, 83–85. [\[CrossRef\]](#)
8. Ioffe, A. *Semiconductor Thermoelements and Thermoelectric Cooling*; Infosearch Ltd.: London, UK, 1957.
9. Terasaki, I. Introduction to thermoelectricity. In *Materials For Energy Conversion Devices*; Woodhead Publishing: Cambridge, UK, 2005; pp. 339–357.
10. Uher, C. Skutterudites: Prospective novel thermoelectrics. *Semiconduct. Semimet.* **2001**, *69*, 139–253.
11. Slack, G.A. New Materials and Performance Limits for Thermoelectric Cooling. In *CRC Handbook of Thermoelectrics*; CRC: Boca Raton, FL, USA, 1995; Chapter 34, pp. 407–440.
12. Takabatake, T.; Suekuni, K.; Nakayama, T.; Kaneshita, E. Phonon-glass electron-crystal thermoelectric clathrates: Experiments and theory. *RMP* **2014**, *86*, 669. [\[CrossRef\]](#)
13. Snyder, G.; Toberer, E. Complex thermoelectric materials. *Nat. Mater.* **2008**, *7*, 105–114. [\[CrossRef\]](#)
14. Toberer, E.; May, A.; Snyder, G. Zintl chemistry for designing high-efficiency thermoelectric materials. *Chem. Mater.* **2010**, *22*, 624–634. [\[CrossRef\]](#)
15. Fleischer, M. The abundance and distribution of the chemical elements in the earth's crust. *J. Chem. Educ.* **1954**, *31*, 446. [\[CrossRef\]](#)
16. Goldsmid, H.; Douglas, R. The use of semiconductors in thermoelectric refrigeration. *Br. J. Appl. Phys.* **1954**, *5*, 386. [\[CrossRef\]](#)
17. Bulusu, A.; Walker, D. Review of electronic transport models for thermoelectric materials. *Superlattices Microstruct.* **2008**, *44*, 1–36. [\[CrossRef\]](#)
18. Tervo, J.; Manninen, A.; Ilola, R.; Hänninen, H. *State-of-the-Art of Thermoelectric Materials Processing*; VTT Working Papers: 124; VTT Technical Research Center of Finland: Espoo, Finland, 2009; ISBN 978-951-38-7184-0.
19. Witting, I.; Chasapis, T.; Ricci, F.; Peters, M.; Heinz, N.; Hautier, G.; Snyder, G. The thermoelectric properties of bismuth telluride. *Adv. Electron. Mater.* **2019**, *5*, 1800904. [\[CrossRef\]](#)
20. Kuhlmann, A. The second most abundant element in the earth's crust. *JOM* **1963**, *15*, 502–505. [\[CrossRef\]](#)
21. Currao, A.; Wengert, S.; Nesper, R.; Curda, J.; Hillebrecht, H. $\text{Ca}_{14}\text{Si}_{19}$ —A Zintl Phase with a Novel Twodimensional Silicon Framework. *Z. Anorg. Allg. Chem.* **1996**, *622*, 501–508. [\[CrossRef\]](#)

22. Currao, A. Synthese, Struktur und Eigenschaften von Zintlphasen der Erdalkali- und Alkali-Erdalkalimetalle mit Silicium. 1996. Available online: <https://www.research-collection.ethz.ch/bitstream/handle/20.500.11850/142715/1/eth-40372-01.pdf> (accessed on 1 December 2022).
23. Manfrinetti, P.; Fornasini, M.; Palenzona, A. The phase diagram of the Ca–Si system. *Intermetallics* **2000**, *8*, 223–228. [\[CrossRef\]](#)
24. Canepa, F.; Napoletano, M.; Manfrinetti, P.; Palenzona, A. Heat capacity and thermodynamic properties of some Ca silicides. *J. Alloys Compd.* **2000**, *299*, 20–23. [\[CrossRef\]](#)
25. Brutti, S.; Ciccioli, A.; Balducci, G.; Gigli, G.; Manfrinetti, P.; Napoletano, M. Thermodynamic stabilities of intermediate phases in the Ca–Si system. *J. Alloys Compd.* **2001**, *317*, 525–531. [\[CrossRef\]](#)
26. Gröbner, J.; Chumak, I.; Schmid-Fetzer, R. Experimental study of ternary Ca–Mg–Si phase equilibria and thermodynamic assessment of Ca–Si and Ca–Mg–Si systems. *Intermetallics* **2003**, *11*, 1065–1074. [\[CrossRef\]](#)
27. Wen, C.; Kato, A.; Nonomura, T.; Tatsuoka, H. Phase selection during calcium silicide formation for layered and powder growth. *J. Alloys Compd.* **2011**, *509*, 4583–4587. [\[CrossRef\]](#)
28. Tao, X.; Yang, J.; Xi, L.; Ouyang, Y. First-principles investigation of the thermo-physical properties of Ca_3Si_4 . *J. Solid State Chem.* **2012**, *194*, 179–187. [\[CrossRef\]](#)
29. Yaokawa, R.; Nakano, H.; Ohashi, M. Growth of CaSi_2 single-phase polycrystalline ingots using the phase relationship between CaSi_2 and associated phases. *Acta Mater.* **2014**, *81*, 41–49. [\[CrossRef\]](#)
30. Eckerlin, P.; Meyer, H.; Wölfel, E. Die Kristallstruktur von CaSn und CaGe . *Z. Anorg. Allg. Chem.* **1955**, *281*, 322–328. [\[CrossRef\]](#)
31. Nedumk, athil, R.; Benson, D.E.; Grins, J.; Spektor, K.; Haussermann, U. The 3R polymorph of CaSi_2 . *J. Solid State Chem.* **2015**, *222*, 18–24.
32. Galkin, N.G.; Galkin, K.G.; Goroshko, D.L.; Dotsenko, S.A.; Kropachev, O.V.; Chernev, I.M.; Subbotin, E.Y.; Migas, D.B.; Fogarassy, Z.; Pecz, B. Ca silicide films—Promising materials for silicon optoelectronics. *Jpn. J. Appl. Phys.* **2023**, *62*, SD0803. [\[CrossRef\]](#)
33. Bordet, P.; Affronte, M.; Sanfilippo, S.; Nunez-Regueiro, M.; Laborde, O.; Olcese, G.L.; Palenzona, A.; Le Floch, S.; Levy, D.; Hanfl, M. Structural phase transitions in CaSi_2 under high pressure. *Phys. Rev. B* **2000**, *62*, 11392–11397. [\[CrossRef\]](#)
34. Imai, M.; Kikegawa, T. Phase Transitions of Alkaline-Earth-Metal Disilicides MAESi_2 (MAE) Ca, Sr, and Ba) at High Pressures and High Temperatures. *Chem. Mater.* **2003**, *15*, 2543–2551. [\[CrossRef\]](#)
35. Evers, J.; Oehlinger, G.; Weiss, A. Effect of pressure on the Structures of Divalent Metal Disilicides MSi_2 , (M = Ca, Eu, Sr). *J. Solid State Chem.* **1977**, *20*, 173–181. [\[CrossRef\]](#)
36. Affronte, M.; Laborde, O.; Olcese, G.L.; Palenzona, A. Low temperature properties of calcium mono- and disilicides. *J. Alloys Compd.* **1998**, *274*, 68–73. [\[CrossRef\]](#)
37. Schwarz, U.; Wosylus, A.; Rosner, H.; Schnelle, W.; Ormeci, A.; Meier, K.; Baranov, A.; Nickals, M.; Leipe, S.; Muller, C.J.; et al. Dumbbells of Five-Connected Silicon Atoms and Superconductivity in the Binary Silicides MSi_3 (M = Ca, Y, Lu). *J. Am. Chem. Soc.* **2012**, *134*, 13558–13561. [\[CrossRef\]](#) [\[PubMed\]](#)
38. Wosylus, A.; Prots, Y.; Burkhardt, U.; Schnelle, W.; Schwarz, U. High-pressure synthesis of the electron-excess compound CaSi_6 . *Sci. Technol. Adv. Mater.* **2007**, *8*, 383–388. [\[CrossRef\]](#)
39. Moll, A.; Viennois, R.; Hermet, P.; Haidoux, A.; Bantignies, J.; Beaudhuin, M. Stability and properties of the friendly environmental Zintl phases: Ca_3Si_4 and $\text{Ca}_{14}\text{Si}_{19}$. *Acta Mater.* **2017**, *125*, 490–497. [\[CrossRef\]](#)
40. Lebegue, S.; Arnaud, B.; Alouani, M. Calculated quasiparticle and optical properties of orthorhombic and cubic Ca_2Si . *Phys. Rev. B* **2005**, *72*, 085103. [\[CrossRef\]](#)
41. Yang, Z.; Shi, D.; Wen, B.; Melnick, R.; Yao, S.; Li, T. First-principle studies of Ca–X (X=Si,Ge,Sn,Pb) intermetallic compounds. *J. Solid State Chem.* **2010**, *183*, 136–143. [\[CrossRef\]](#)
42. Migas, D.; Shaposhnikov, V.; Filonov, A.; Dorozhkin, N.; Borisenko, V. New semiconducting silicide Ca_3Si_4 . *J. Phys. Condens. Matter* **2007**, *19*, 346207. [\[CrossRef\]](#)
43. Wen, C.; Nonomura, T.; Warashina, Y.; Kubota, Y.; Nakamura, T.; Hayakawa, Y.; Tanaka, M.; Isobe, K.; Tatsuoka, H. Synthesis of single-phase polycrystalline Ca_2Si powder and sintered compacts. *Int. J. Mater. Res.* **2011**, *102*, 401–405. [\[CrossRef\]](#)
44. Wen, C.; Nonomura, T.; Isobe, K.; Kubota, Y.; Nakamura, T.; Hayakawa, Y.; Kato, A.; Tatsuoka, H. Effect of Na Addition on Electric Properties of Ca_2Si Sintered Compacts. *IOP Conf. Ser. Mater. Sci. Eng.* **2011**, *18*, 142014. [\[CrossRef\]](#)
45. Jun, C.; Yin, Y.; Yi, L.; Quan, X.; Jinmin, Z. Selective Growth of Ca_2Si Film or Ca_5Si_3 Film in Ca–Si System by R.F MS by Annealing. In Proceedings of the 2012 International Conference on Manipulation, Manufacturing and Measurement on the Nanoscale (3M-NANO), Xi'an, China, 29 August–1 September 2012; pp. 75–79.
46. Inaba, T.; Kato, A.; Miura, K.; Akasaka, M.; Iida, T.; Momose, Y.; Tatsuoka, H. Preparation and electrical properties of Ca_5Si_3 and Sr_5Si_3 powders. *Thin Solid Films* **2007**, *515*, 8226–8229. [\[CrossRef\]](#)
47. Uhera, M.; Akiyama, K.; Shimizu, T.; Matsushima, M.; Uchida, H.; Kimura, Y.; Funakubo, H. Preparation of Ca–Si Films on (001) Al_2O_3 Substrates by an RF Magnetron Sputtering Method and Their Electrical Properties. *J. Electron. Mater.* **2016**, *45*, 3121–3126. [\[CrossRef\]](#)
48. Imamura, Y.; Muta, H.; Kurosaki, K.; Yamanaka, S. Thermoelectric properties of calcium silicides. In Proceedings of the 2006 25th International on Thermoelectrics, Vienna, Austria, 6–10 August 2006; pp. 535–538.
49. Snyder, G.J. Zintl Phases: Recent Developments in Thermoelectrics and Future Outlook. *Thermoelectr. Mater. Devices* **2016**, *1*. [\[CrossRef\]](#)

50. Dudina, D.V.; Mukherjee, A.K. Reactive spark plasma sintering: Successes and challenges of nanomaterial synthesis. *J. Nanomat.* **2013**, *2013*, 625218. [[CrossRef](#)]
51. Mukasyan, A.S.; Rogachev, A.S.; Moskovskikh, D.O.; Yermekova, Z.S. Reactive spark plasma sintering of exothermic systems: A critical review. *Ceram. Int.* **2022**, *48*, 2988–2998. [[CrossRef](#)]
52. Munir, Z.; Anselmi-Tamburini, U.; Ohyanagi, M. The effect of electric field and pressure on the synthesis and consolidation of materials: A review of the spark plasma sintering method. *J. Mater. Sci.* **2006**, *41*, 763–777. [[CrossRef](#)]
53. Hu, Z.-Y.; Zhang, Z.-H.; Cheng, X.-W.; Wang, F.-C.; Zhang, Y.-F.; Li, S.-L. A review of multi-physical fields induced phenomena and effects in spark plasma sintering: Fundamentals and applications. *Mater. Des.* **2020**, *191*, 108662.
54. Manière, C.; Nigito, E.; Dur, L.; Weibel, A.; Beynet, Y.; Estournès, C. Spark plasma sintering and complex shapes: The deformed interfaces approach. *Powder Technol.* **2017**, *320*, 340–345. [[CrossRef](#)]
55. Elissalde, C.; Chung, U.-C.; Josse, M.; Goglio, G.; Suchomel, M.R.; Majimel, J.; Weibel, A.; Soubie, F.; Flaureau, A.; Fregeac, A.; et al. Single-step sintering of zirconia ceramics using hydroxide precursors and Spark Plasma Sintering below 400 °C. *Scr. Mater.* **2019**, *168*, 134–138. [[CrossRef](#)]
56. de Beauvoir, T.H.; Ghomari, Z.; Chevallier, G.; Flaureau, A.; Weibel, A.; Elissalde, C.; Mauvy, F.; Chaim, R.; Estournès, C. Flash Spark Plasma Sintering of 3YSZ: Modified sintering pathway and impact on grain boundary formation. *J. Eur. Cer. Soc.* **2021**, *41*, 7762–7770. [[CrossRef](#)]
57. Rahaman, M. *Sintering of Ceramics*; CRC Press: Boca Raton, FL, USA, 2007.
58. Abbassi, L.; Mesguich, D.; Coulomb, L.; Chevallier, G.; Aries, R.; Estournès, C.; Flahaut, E.; Viennois, R.; Beaudhuin, M. In-situ reactive synthesis of dense nanostructured β -FeSi₂ by Spark Plasma Sintering. *J. Alloys Compd.* **2022**, *902*, 163683. [[CrossRef](#)]
59. Lyu, J.; Kashkarov, E.B.; Travitzky, N.; Syrtanov, M.S.; Lider, A.M. Sintering of MAX-phase materials by spark plasma and other methods. *J. Mater. Sci.* **2021**, *56*, 1980–2015. [[CrossRef](#)]
60. Gild, J.; Kaufmann, K.; Vecchio, K.; Luo, J. Reactive flash spark plasma sintering of high-entropy ultrahigh temperature ceramics. *Scr. Mater.* **2019**, *170*, 106–110. [[CrossRef](#)]
61. Rodriguez-Carvajal, J.; Roisnel, T. *FullProf-98 and WinPLOTR: New Windows 95/NT Applications for Diffraction Commission for Powder Diffraction*; International Union of Crystallography: Chester, UK, 1998.
62. Pauw, L. A method of measuring the resistivity and Hall coefficient on lamellae of arbitrary shape. *Philips Tech. Rev.* **1958**, *20*, 220–224.
63. Blundell, S.; Blundell, K. *Concepts in Thermal Physics*; Oxford University Press: Oxford, UK, 2010.
64. Ali, D.O.A.; Fabbiani, M.; Koza, M.M.; Beaudhuin, M.; Viennois, R. Inelastic neutron scattering study of the lattice dynamics of the green semiconducting calcium silicides for thermoelectric applications. **2022**. *Unpublished Work*.
65. Bandhari, C.M.; Rowe, D.M. Optimization of Carrier Concentration. *CRC Handbook of Thermoelectrics*; CRC: Boca Raton, FL, USA, 1995; Chapter 5.
66. Borisenko, V. E. *Semiconducting Silicides*; Springer Series in Material Science, 39; Springer: Berlin/Heidelberg, Germany, 2000.

Disclaimer/Publisher’s Note: The statements, opinions and data contained in all publications are solely those of the individual author(s) and contributor(s) and not of MDPI and/or the editor(s). MDPI and/or the editor(s) disclaim responsibility for any injury to people or property resulting from any ideas, methods, instructions or products referred to in the content.